ORIGINAL PAPER

Lanthanide and yttrium substitution in natural fluorite

Nicola J. Horsburgh[1] · Adrian A. Finch[1] · Henrik Friis[2]

Abstract

Fluorite is one of the most common minerals in the crust and is of widespread economic importance. It shows strong UV-excited luminescence, variously attributed to defects within the fluorite structure and lanthanide substitutions. We present here a detailed chemical characterisation of a suite of natural fluorite samples, chosen to represent the range of compositions observed in nature. We perform X-ray excited luminescence spectroscopy on the samples as a function of temperature (20–673 K) in the wavelength range 250–800 nm to provide insights into physical defects in the lattice and their interactions with lanthanide substituents in natural fluorite. Most broad bands in the UV are attributed to electronic defects in the fluorite lattice, whereas sharp emissions are attributed to intra-ion energy cascades in trivalent lanthanides. Lanthanides are accommodated in fluorite by substitution for Ca^{2+} coupled with interstitial F^-, O^{2-} (substituting for F^-) and a variety of electronic defect structures which provide local charge balance. The chondrite-normalised lanthanide profiles show that fluorite accommodates a greater proportion of heavy lanthanides (and Y) as the total Rare Earth Element (REE) concentration increases; whereas cell parameters decrease and then increase as substitution continues. Luminescence intensity also goes through a maximum and then decreases as a function of REE concentration. All three datasets are consistent with a model whereby lanthanides initially act as isolated centres, but, beyond a critical threshold (~ 1000 ppm), cluster into lanthanide-rich domains. Clustering results in shorter REE-O bond distances (favouring smaller heavier ions), a larger unit cell but more efficient energy transfer between lanthanides, thereby promoting non-radiative energy loss and a drop in the intensity of lanthanide emission.

Keywords XEOL · Radioluminescence · Defect clustering · Lanthanides · Rare earths

Introduction

Fluorite (CaF_2) is a naturally occurring, cubic, wide band-gap, ($E_g = 12.2$ eV, Assylbayev et al. 2018) ionic crystalline solid which is used in the production of hydrofluoric acid (HF), as a flux in metallurgy and for several applications including ceramic glazes, optics, radiation dosimetry and vacuum ultraviolet components (Aoki et al. 2015). In addition, fluorite is considered in EU surveys as a 'critical raw material' for European industries. Natural fluorite contains many trace elements, including significant concentrations of Rare Earth Elements (REE = lanthanides + Y) which

modify the spectroscopy of the fluorite including its colour and luminescence. Fluorite emits a characteristic light when irradiated by UV and the term 'fluorescence' was first coined for this behaviour by Stokes from studying fluorite (Stokes 1852; Valeur and Berberan-Santos 2011).

The present paper analyses a suite of natural fluorites to provide insights into the effects of lanthanide substitution on the luminescence of natural fluorite. We explore fluorescence as a function of temperature from 20 to 673 K, exciting the samples using X-irradiation (variously called Radio-Luminescence, RL or X-ray Excited Optical Luminescence, XEOL). We analyse the data not only to provide insights into emissions resulting from lanthanide substitution, but also to understand how coupling of structural defects and lanthanides takes place. In doing so, we provide new insights into the defect structures of natural fluorite, one of the world's most important critical raw materials.

✉ Adrian A. Finch
    aaf1@st-andrews.ac.uk

[1] School of Earth and Environmental Sciences, University
     of St. Andrews, St. Andrews KY16 9AL, Scotland

[2] Natural History Museum, University of Oslo, Blindern,
     P.O. 1172, 0318 Oslo, Norway

Materials and methods

Samples

Most natural REE-rich fluorites form during late-stage magmatic or hydrothermal activity associated with evolved igneous bodies, and therefore, we focus on samples from that paragenesis in the present study. All have affinity with magmatism either from alkaline or granitic settings. The samples studied here are chosen as a subset that represents a cross section of colour, chemical variation and UV response in fluorite. The provenance of the samples is summarised in Table 1 but the key features are as follows: Greenland samples (NJH-16-39ppl and NJH-16-41grn) were collected from the Motzfeldt Complex, Gardar Province, South Greenland, an alkaline igneous setting (Finch et al. 2019a). The area represents the emplacement of Early Gardar rift related alkaline magmatism dating from 1320 to 1270 Ma (Upton et al. 2003; Upton 2013). Fluorite is found in veins and were collected from a vein in loose material near 1300 m summit, a down faulted block of Eriksfjord trachytes, interpreted as a preserved roof zone rich in volatile fluids (Finch et al. 2001, 2019a).

Fluorite samples from Norway are from typical Niobium–Yttrium–Fluorine (NYF) pegmatites associated with granitic intrusions. Hundholmen and Nedre Eivollen are within the Trans-Scandinavian igneous belt, hosted by and associated with the Tysfjord Granite which is dated 1810–1660 Ma (Müller et al. 2017; Romer et al. 1992). Aspedammen fluorite comes from the county of Østfold, within the border zone between the Iddefjord granite (~ 900 Ma) and the neighbouring gneiss complex (~ 1800 Ma) within the Norwegian Precambrian shield (Cooper et al. 2012). Hundholmen and Nedre Eivollen fluorites are catalogued as yttrofluorite (a Y rich variety of fluorite, Vogt 1923; Sverdrup 1968) in the collections of the Natural History Museum in Oslo. This term is inconsistently used in the literature to indicate fluorite with REE enrichment but, as recommended by Pekov et al. (2009), we use the term yttrofluorite for fluorite with total REE oxide values > 2%. Tveitite-(Y), ideally $(Y, Na)_6(Ca, Na, REE)_{12}(Ca, Na)F_{42}$, is a trigonal mineral, whose structure is based upon a stuffed fluorite structural template (Bergstøl et al. 1977; Bevan et al. 1982; Pekov et al. 2009). Despite the high Y content of some samples in this study, XRD investigations show them all to have the fluorite structure. Material from all samples is archived in collections at the University of St Andrews.

Electron probe microanalysis (EPMA)

Ca, F, Y, La and Ce were measured by wavelength-dispersive spectroscopy (WDS) using a CAMECA SX100 electron probe micro-analyser (EPMA) at the University of Edinburgh, United Kingdom. Samples were measured using an acceleration voltage of 15 kV and larger beam size of 10 μm diameter to decrease the incident beam power density and thereby minimise loss of volatile elements. The beam current was set to 2 nA for Ca and F, and 60 nA for Y, La and Ce. Counting times were 10 s on peak, with half that off peak. Calibration standards were Calcite-Silicarb (Ca Kα), fluorite (F Kα) and synthetic REE-phosphates (La Lα, Ce Lβ, Y Kα). The data were reduced and corrected using the PAP routine (Pouchou and Pichoir 1984). Although we present EPMA data here only for Ca and Y, we estimated other minor elements at the time to ensure that matrix corrections were optimised. During WDS, qualitative Energy-Dispersive X-ray Analysis (EDXA) of secondary X-rays was performed to check whether significant amounts of S and Cl were present; those elements were not observed. The primary purpose of EPMA was to provide estimates of Ca from which to normalise LA-ICP-MS data (see below). We consider the estimates of Y in yttrofluorite to be more accurate by EPMA since saturation of the detectors by ICP-MS was observed.

Table 1 Physical characteristics (colour and UV fluorescence) and provenance of samples

Sample	Colour	UV A (365 nm)	UV C (254 nm)	Provenance	Source
NJH-16-39ppl	Purple	–	–	Motzfeldt Centre, Igaliku Complex, Kujalleq, Greenland	Collected by NJH
NJH-16-41grn	Green	Blue/purple	Blue/purple	Motzfeldt Centre, Igaliku Complex, Kujalleq, Greenland	Collected by NJH
Aspedammen	Dark green	Green	Yellow	Aspedammen, Østfold, Norway	Oslo NHM exchange collection
Hundholmen	Pale yellow/green	Yellow	Yellow	Hundholmen, Tysfjord, Nordland, Norway	Oslo NHM exchange collection
Nedre Eivollen	Pink	White/yellow	White	Nedre Eivollen, Drag, Tysfjord, Nordland, Norway	Oslo NHM exchange collection

The colour is replicated on geochemical figures below to give an intuitive sense of the sample referred to

Laser ablation inductively coupled mass spectrometry (LA-ICPMS)

Trace elements were measured by LA-ICP-MS at the School of Earth and Environmental Sciences, University of St Andrews, UK. The system comprises an UP213 New Wave frequency quintupled Nd:YAG Laser system attached to a quadrupole-based Thermo X'Series II ICPMS. Ablation was performed at a rate of 20 Hz and a constant energy of ~ 10 J cm^{-2}, with He was used as a carrier gas (Eggins 1998) and mixed with Ar on entering the chamber to aid stability. NIST612 glass was used as an external calibration sample. Data were processed offline using Pepita software (Dunkl et al. 2008) using Ca (determined by EPMA, see above) as an internal standard element. For estimates of Y concentration in yttrofluorite, we consider the data by EPMA to be more accurate since saturation of the detectors by LA-ICP-MS is anticipated. This instrument has typical precision (to 95% confidence) of $\pm$ 10% of the mean and limits of detection (lod) range between 1 and 3 ppm. In the present study, any data shown in ppm are taken from LA-ICPMS and the associated precision to 95% confidence interval can be inferred to be 10% of the mean.

X-ray diffraction (XRD)

Single-crystal fragments of each sample were mounted on a Rigaku Synergy-S diffractometer equipped with a HyPix-6000HE detector housed at the Natural History Museum, University of Oslo, Norway. A PhotonJet-S microfocus sealed tube operating at 50 kV and 1 mA provided the monochromatic Mo Kα-radiation. Diffraction data were collected at room temperature and the CrysAlis Pro software was used for data processing and unit cell refinement.

Luminescence spectroscopy

Fluorite samples were examined using short (UV-C 254 nm) and long (UV-A 365 nm) UV light using an Analytik Jena mineralogical UV lamp. Samples were examined visually to determine fluorescence response and to identify a range of emission for further examination using high sensitivity instrumentation. X-ray Excited Optical Luminescence (XEOL) measurements were made on a high sensitivity luminescence spectrometer system at the University of St Andrews, UK (Finch et al. 2019b) using single crystal fragments. X-rays are chosen above other forms of excitation because this radiation penetrates deeply into the crystal and delivers a response that is representative of the bulk, in contrast to e.g. cathodoluminescence, where luminescence is dominated by atypical surface responses. We therefore probe the bulk crystalline solid with our experiments. Cryogenic measurements are made on a low temperature stage that operates from 20 to 300 K. The samples are cooled to 20 K then heated, while high-temperature measurements are made from 300 to 673 K on a separate stage. A ramp rate of 6 K min^{-1} is used to minimise thermal lag between the thermocouple and the sample (Betts and Townsend 1993; Townsend et al. 1997; Ege et al. 2007) with continuous X-irradiation. The X-ray source is a Philips MCN-101 ceramic X-ray tube typically running at 20 kV and 20 mA delivering X-rays at 20 Gy min^{-1}. Data collected were processed using custom made software and further details on processing and the instrument are given by Finch et al. (2019b).

Results

Fluorite geochemistry and crystallography

Natural fluorite is typically > 99% CaF$_2$ (Chang et al. 1996), although the samples in the present study are atypical and chosen to include those with elevated REE. The cell parameters and chemical compositions of the samples are given in Table 2. The cell parameters show a shrinking and then expansion of the unit cell as a function of total RE content (Fig. 1), with the inflection point ~ 2000 ppm. Chondrite normalised REE (including Y) profiles are provided in Fig. 2. Elemental substitution in the samples of the present study range by orders of magnitude from NJH-16-39ppl, (which has a sum of all substituents of 400 ppm = 0.04%) ranging to 18.4% in Nedre Eivollen.

Short/long wave UV

The colour of the samples in hand specimen and the visible fluorescence on exposure to short and long wave UV is summarised in Table 1. The dark purple fluorite shows no visible fluorescence in either the UVA or UVC. However, most samples show responses in both ranges, although the colour of that response is not the same for Aspedammen fluorite, which is green in UVA and yellow under UVC.

X-ray excited optical luminescence (XEOL)

XEOL data at high and low temperature are shown as contour plots in Fig. 3. A summary of the main findings is presented below.

NJH-16-39ppl (fluorite)

Many trace elements in this sample, including the lanthanides are at or below the limit of detection for LA-ICPMS, and this sample is the purest fluorite analysed in the

Table 2 Unit cell parameter and Chemical compositions of the samples

|	NJH-16-39ppl	NJH-16-41grn	Aspedammen	Hundholmen (yttrofluorite)	Nedre Eivollen (yttrofluorite)
Cell parameter					
a (Å)	5.4684 (6)	5.4659 (5)	5.4664 (8)	5.4872 (7)	5.5001 (5)
Compositions					
Ca	52.29%	51.86%	51.89%	39.35%	42.30%
Na	<lod	<lod	147	655	1167
Mg	<lod	2	3	2	3
Mn	<lod	3	528	6	11
Fe	<lod	82	<lod	<lod	<lod
Co	36	53	49	25	10
Zn	<lod	<lod	2	1	<lod
Sr	267	321	7	108	143
Y	75	831	1137	*8.78%*	*8.51%*
Zr	<lod	2	<lod	<lod	<lod
Nb	<lod	6	<lod	<lod	<lod
La	4	46	7	139	5781
Ce	5	75	21	153	9740
Pr	2	15	7	38	2074
Nd	4	83	47	361	12,400
Sm	1	42	170	424	5486
Eu	<lod	2	1	4	1
Gd	2	42	322	2208	9362
Tb	<lod	7	75	599	1809
Dy	4	45	211	5773	14,200
Ho	1	6	7	1606	3590
Er	5	19	5	5507	12,300
Tm	<lod	2	<lod	901	2133
Yb	1	14	3	5811	15,600
Lu	<lod	2	<lod	952	2548
Hf	<lod	<lod	<lod	3	7
Ta	<lod	<lod	<lod	<lod	2
Th	<lod	4	16	2	35
∑REE% (not incl Y)	0.01%	0.1%	0.1%	2%	9%
Atomic Na: ∑REE	Na n.d.	Na n.d.	2:5	1:25	1:25
∑Substitution elements %	0.04%	0.1%	0.25%	11%	18%

Cell parameters are calculated from refinement of XRD data, the precision in the last digit is in parentheses. Compositional data shown in % are measured by EPMA whereas those presented without a unit are in ppm and estimated by LA-ICPMS using Ca as internal standard. Data are typically the averages of 4 replicate runs. K, Sc, Ti, V, Cr, Ni, Cu, Ga, Mo, Ba, U are all below limit of detection by LA-ICP-MS. Precision in Ca EPMA data are typically 0.5% (to 95% CI) whereas LA-ICP-MS data is~ ± 10% of the mean. Lod by LA-ICP-MS is typically 1–3 ppm

present study. Sr (267 ppm), Y (75 ppm) and Co (36 ppm) are the only substituents present in detectable concentrations. The XEOL shows strong UV/blue emission in the low temperature (20–300 K) spectra centred in one broad band with the maximum intensity at 282 nm. Above 373 K the UV emission reduces in intensity and the narrower emission line at 480 nm becomes more dominant.

NJH-16-41grn (fluorite)

Numerous trace elements are present and this is the only sample with measurable Fe (82 ppm), Zr (2.1 ppm) and Nb (5.9 ppm). The most abundant trace elements are Sr (321 ppm) and rare earths (831 ppm) with individual lanthanides detectable ranging from 83 to 2.0 ppm. Th is above lod at 4.1 ppm. The low temperature XEOL is dominated by

Fig. 1 Cell parameter (a) versus total rare earth content. The colour of the symbols relates to the colour of the sample, e.g. purple fluorite is represented by a purple symbol. The fine line is a linear fit through the last three points. The error in both parameters lies within the magnitude of the symbol. The cell shrinks as lanthanides are added to the structure up to ~2000 ppm at which point it expands linearly with total REE content
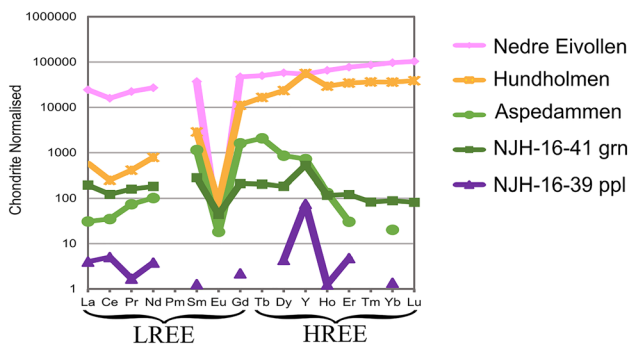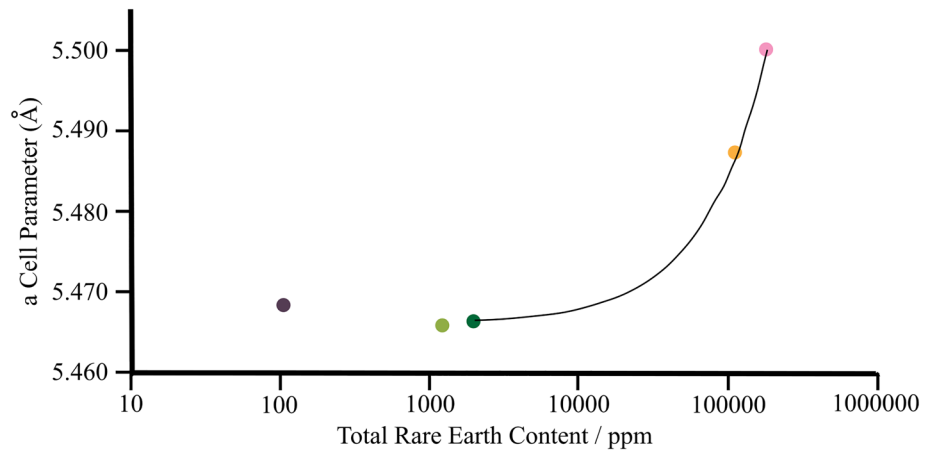
Fig. 2 Chondrite (C1) normalised Rare Earth Profiles (*Y* is plotted between Dy and Ho) of fluorite in this study. Values below LOD are not plotted. The Light Rare Earth Element (LREE) and Heavy Rare Earth Element (HREE) series are indicated. Chondrite values are from McDonough and Sun (1995). The symbol colour represents the colours of the samples in hand specimen

a strong UV blue emission at 20 K centred around 280 nm, with additional narrow emission bands at 320, 380, 480, 540, 560, 580 and 600 nm. At 65 K the strong UV/blue emission abruptly becomes more intense and emits over a wider wavelength (from 250 to 340 nm), the narrower emission bands also increase in intensity and broaden, with additional narrow bands becoming visible around 670 nm and 760 nm. At 245 K the intensity reduces for nearly all emissions and all samples. The most intense emission switches at 200 K to 312, which peaks at 220 K alongside the emissions at 340, 380, 416 and 480 nm. From 240 to 300 K the emission across the spectra becomes weaker. High temperature XEOL is dominated by peaks at 250–300, 380, 416 and 480 nm between 473 and 633 K. There is an abrupt reduction in signal at 646 K caused by decrepitation of the crystal.

Aspedammen (fluorite)

Aspedammen fluorite shows trace element substitutions with Y (1137 ppm), Mn (528 ppm), Na (147 ppm), Co (49 ppm) and Th (17 ppm) all present at notable concentrations. The lanthanide concentrations are e.g. Ce = 22 ppm, Sm = 170 ppm and Dy = 211 ppm, with the sample showing REE enrichment centred around Tb (Fig. 2). Low temperature XEOL is dominated by bands at 280, 310, 382, 413, 438, 495 and 566 nm, with the strongest emission at 495 nm. At high temperatures the XEOL shows the most intense emission at 485 nm with the additional narrow bands at 470, 532 and 560 nm. A peak in intensity can be seen at 485 nm, from 500 to 600 K.

Hundholmen (yttrofluorite)

Substantial substitution of the lanthanides is present with notable enrichment in HREE (Gd 2208 ppm, Dy 5773 ppm and Yb 5810 ppm). Na (117 ppm) and Sr (655 ppm) are also significantly above lod. This sample contains 8.8% Y, and 2.35% ΣREE (excluding Y). XEOL at low temperature shows numerous narrow emission bands at 312, 381, 400, 414, 440, 476, 540, 568 and 621 nm. The bands in the UV/ blue regions narrow and reduce in intensity above 100 K while the intensity of the 480 nm band intensifies. The spectra at high temperatures show stronger emissions from the green and yellow regions (i.e. 480, 543, 573 nm). In the UV/ blue there is a broader emission at 322 nm which peaks in intensity between 450 and 600 K. An emission is also present centred around 280 nm at 20 K (seen as a sideband to the sharp line at 311 nm) which fades on heating to 175 K, beyond which the feature is no longer visible.

Nedre eivollen (yttrofluorite)

Y (8.5%) and some lanthanides are present as major elements (Ce 9740 ppm, Nd 12,417 ppm, Dy 14,248 ppm, Gd 9362 ppm, Er 12,300 ppm, Yb 15,600 ppm) and this sample is particularly enriched in HREE. Na is present at just over 1% (1117 ppm). Sr (142 ppm) and Th (35 ppm) are also present at significant concentrations. XEOL spectra at
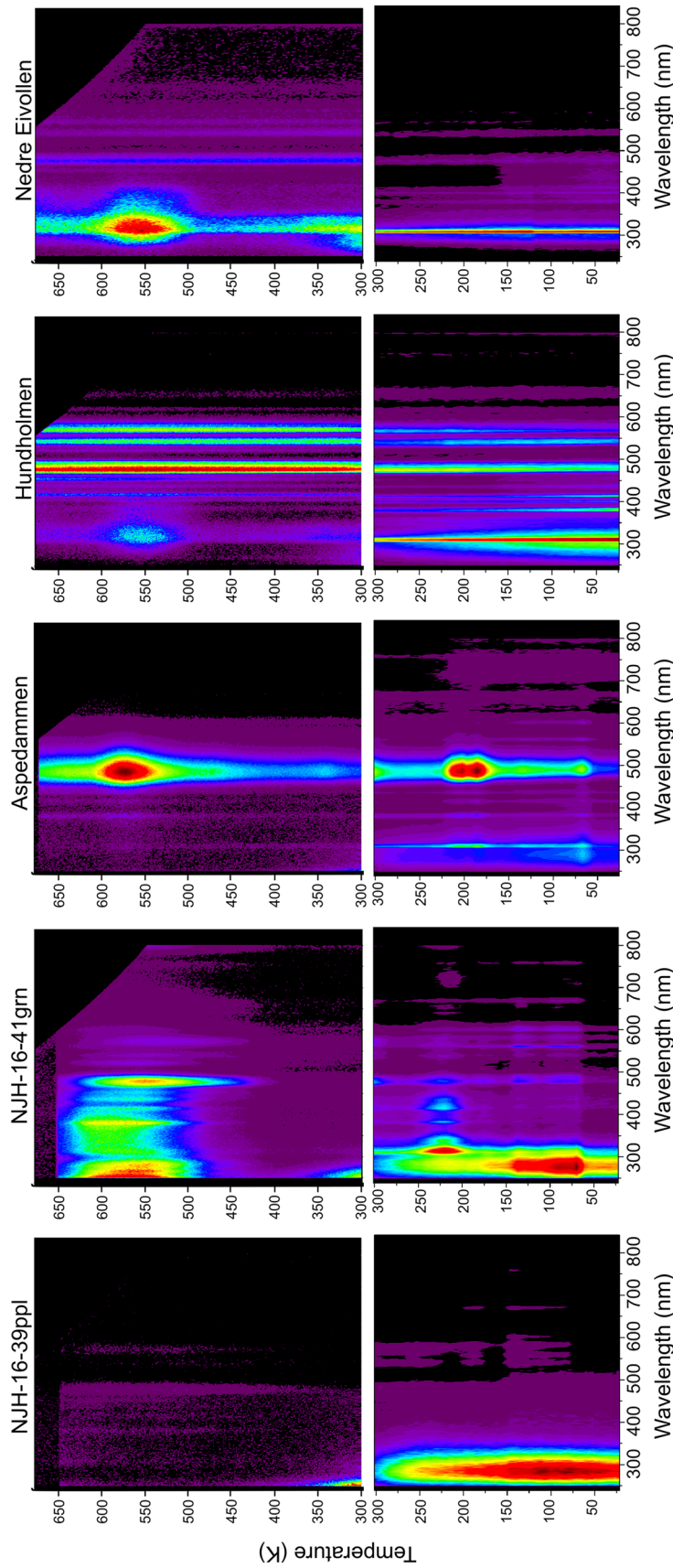
Fig. 3 XEOL as a function of temperature for the samples in Table 1. Data are shown as contour plots with hot colours (orange-red) representing high counts and cold colours (black, purple) fewer counts. The bottom row shows cryogenic data 20–300 K whereas the top row shows high temperature data from 300 to 673 K (400 °C). Typically intensity is greater at lower temperature but the colour intensities of the two ranges are normalised independently. This often results in a slight discontinuity across the high and low temperature graphs

low temperature display emissions from UV to green with the main bands centred around 310, 382, 415, 438, 480 and 540 nm. Intensity of emission increases across the spectra at 120 K, reducing gradually on further heating. A peak at 440 nm is observed from 20 K, reducing in intensity until it stops abruptly at 150 K when an emission line at 560 nm begins to emit at higher temperatures. High temperature data shows emission lines at 280, 311, 473, 550 and and 574 nm. The most intense is noted from the 311 nm line which shows dramatic broadening and a secondary shoulder peak at 320 nm when the intensity increases at 500 K.

Discussion

F constitutes the only anion detected by any of our methods, but it is important to note that oxygen was not analysed directly by EPMA and our ICPMS analyses were configured only to measure species which form positive ions. Limits of detection by ICPMS are orders of magnitude higher for anions using the methods applied. It may therefore be that oxide ions or other elements such as Cl or S are present but undetected in the fluorites, although neither of the latter were observed in routine EDXA analysis taken alongside WDS EPMA analyses. Most of the elements observed are metals and it is inferred that they substitute for Ca^{2+} in the Ca site. Mg and Sr are divalent and we infer that these substitute directly for Ca^{2+}. Similarly, the transition metals Fe, Mn and Co each have divalent forms which we infer substitute homovalently for Ca^{2+}. Substitution of divalent ions causes physical distortions as smaller or larger ions occupy the site. The degree of distortion depends on the 'stiffness' of the site, expressed by the Young's Modulus (Blundy and Wood 1994). Ionic solids such as fluorite have flexible structures (low Young's Modulus) that distort relatively easily when substitutions take place. Such structures tend to accommodate a wide range of substituent ions (Table 2).

The other metals detected are not divalent ions. Na is a 1 + ion, whereas most other metals in the analysis are trivalent rare earths. Charge imbalances caused by Na and REE substitution may be coupled such that: $REE^{3+} + Na^+ \leftrightarrow 2Ca^{2+}$, as is the case with apatite (Oberti et al. 2001). However, NJH-16-39 ppl and NJH-16-41-grn have REE but no Na and, for all samples, Na $\ll \Sigma$REE (Table 2). Since the concentrations of Na are far less than atomic ΣREE, coupled exchange with Na is, at best, a minor mechanism to accommodate REE. Because we cannot measure O^{2-} precisely, it may be that a coupled substitution involving REE and oxide is present: $REE^{3+} + O^{2-} \leftrightarrow Ca^{2+} + F^-$ although the analysis of fluorite by EDXA during EPMA analysis did not show significant (i.e. %) amounts of O. We therefore tentatively conclude that this substitution, although likely, is volumetrically small.

REE concentrations exceed those of any discernible coupled substitution, and hence we infer that most charge imbalances caused by the REE are offset by physical and electronic defects that are undetectable by our chemical analyses. This may be, for example, a cation vacancy: $2REE^{3+} + \square \leftrightarrow 3Ca^{2+}$ or extra fluoride ions accommodated interstitially $REE^{3+} + F^-_{(int)} \leftrightarrow Ca^{2+}$ (Cheetham et al. 1971; Bevan et al. 1982). Interstitial fluoride ions are widely considered the primary mechanism by which lanthanides are accommodated in fluorite (see Assylbayev et al. 2018 and refs therein). Frenkel defects in fluorite comprise an interstitial F^- ion coupled to a F vacancy and ab initio calculations suggest that such structures form readily in response to irradiation. Frenkel defects themselves do not create electrostatic imbalances but, as is shown below, they accommodate charge if the fluoride vacancy traps an electron or the interstitial F-attracts an electron hole to create an H-centre (Fig. 4).

The volume of spectroscopic data on natural fluorite is smaller than a larger body of work on the spectroscopy of synthetic alkali and alkaline earth halides (e.g. Bartram and Stoneham 1975; Lopez et al. 1980; Popov et al. 2017) which can inform the present study. In addition to physical defects (vacancies and/or interstitials), a variety of spectroscopic features in synthetic fluorite have been attributed to electronic defects such an extra electrons or electron holes (Stoneham 2001). For example, a common defect in halides is the F-centre where an electron becomes trapped at an anion vacancy. The F-centre forms easily as a highly symmetrical tetrahedral defect in alkaline earth fluorides created during γ or X-ray irradiation (Stoneham 2001), first by creating a Frenkel defect to make an anion vacancy, and then by stabilising the vacancy by the formation of an F-centre. Two F-centres can then form an M centre by clustering and colour in natural fluorite is attributed to absorption in the yellow and violet parts of the spectrum by F and M centres (e.g. Bill and Calas 1978; Dill and Weber 2010; Gaft et al. 2015).

The self-trapped exciton in fluorite (i.e. a paired electron and electron hole) emits at 280 nm (Fig. 3, Table 3) and in fluorite the self-trapped exciton is believed to take the form of an F- and H-centre couple (Song and Williams 1996). Alkali halides also commonly show families of entities accommodating extra electrons and electron holes (Fig. 4), stabilised by delocalising the charge over two or more ions and/or by electrostatically pairing positive and negative defects, which reduce the overall free energy of the pair. For example, V_k centres form in fluorite exposed to radiation—this defect is interpreted as a hole shared by two neighbouring F ions, i.e. $2F^- + h^+ = F_2^-$ and is located across two regular lattice sites along [100] (Fig. 4). H centres are similar but the hole is shared by four F ions in three neighbouring sites (along the 110 axis) (Townsend and Kelly 1973; Agulló-López et al. 1988). When an electron

Fig. 4 Schematic representations of common defects in fluorite, small grey atoms are cations (Ca^{2+}), while larger blue atoms are anions ($F^−$). *F*-centre a fluorine vacancy plus a trapped electron. *M*-centre two adjacent *F*-centres. V_k-centre a hole shared by neighbouring F ions to form an $X_2^−$. *H*-centre is a hole shared by four F ions in 3 neighbouring sites (Adapted from (Agulló-López et al. 1988)
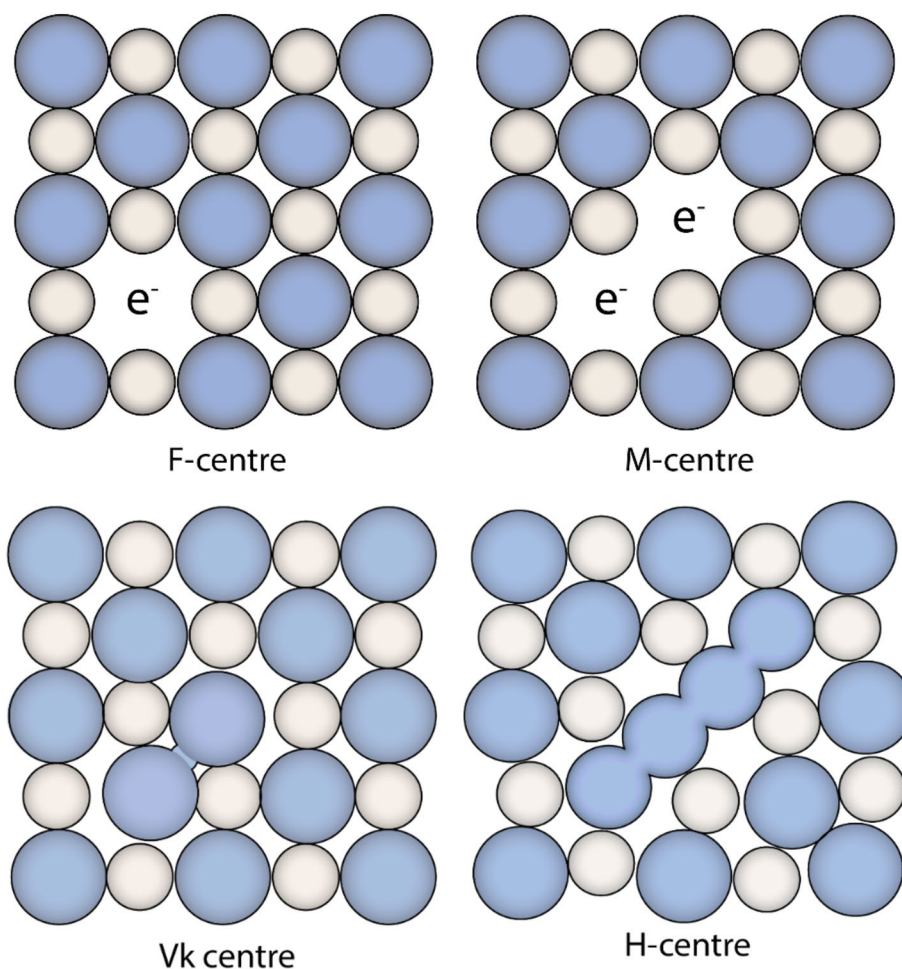
recombines with V_k centre, a clustered metastable defect group forms, comprising a Frenkel pair coupled to two electron holes associated in space with two *F*-centres (electrons trapped at $F^−$ vacancies, Stoneham 2001; Popov et al. 2017). The pairing of positive and negative defects in fluorite hints that physical coupling in space of lanthanide substituents with electronic defects is a credible route to stabilise them. For example, a simple means to accommodate REE^{3+} is to couple it to an extra electron: $REE^{3+} + e^- \leftrightarrow Ca^{2+}$ where the electron is stabilised by a defect structure.

The structures discussed above involve charge delocalisation across defect groupings and the physical coupling in space of substituent ions and electronic defects. We therefore hypothesise that luminescence of natural fluorite (Fig. 3) can be explained by a) intra-ion electronic cascades due to the presence of impurity ions (sometimes called luminescence 'activation' and associated with many REE), b) structural defects (i.e. Self-Trapped Excitons (STE), *F* and M Centres, oxygen defects) and c) the spatial and electronic coupling of chemical and structural defects. During heating of the sample, sudden increases in luminescence intensity are observed at key temperatures (e.g. at 573 K in Aspedammen,

Fig. 3). We interpret these as combinations of XEOL with Thermo-Stimulated Luminescence (TSL, sometimes called Thermoluminescence, TL), i.e. the discharge of energy from electronic point defects as they become unstable at thermal thresholds. A full study of TSL of the samples will be presented in a later communication but we note here that the presence of TSL in fluorite indicates that fluorite accommodates several different electronic point defect types.

Features in luminescence attributed to structural defects

XEOL was recorded for all samples at low (20–300 K) and high (300–673 K) temperatures. Several common features are observed across the fluorites analysed. All but Nedre Eivollen contain a broad emission in the UV, attributed to intrinsic defects within the structure (Dieke and Crosswhite 1963; McKeever and Chen 1997; Yang et al. 1998; Stoneham 2001).

The 280-nm-emission dominates fluorite luminescence when REE content is low (NJH-18-39ppl and NJH-18-41grn) and this is ascribed to the self-trapped exciton on

Table 3 Summary of Luminescence responses, the temperatures of luminescence maxima and the attributed emission centres

Emission (nm)

	STE	Gd³⁺	Ce³⁺	Tb³⁺	Dy³⁺	Sm³⁺	Ce³⁺=O⁻ defect
					476-486		
					576		
				408-440	580		
				490-496	591		
		311	320	536-546	674	561	
	280	312	340	585	754	568	~380

Sample		STE	Gd³⁺	Ce³⁺	Tb³⁺	Dy³⁺	Sm³⁺	Ce³⁺=O⁻ defect	Suggested cause
NJH-16-39ppl	H	>450			450	450		450	Minor Tb and Dy
	L	80, **110**, 140	80, 110, 140	140, 240					Dominated by STE
NJH-16-41grn	H	**>473**	500	500	>473	**>450**		>500	Dominated by STE, Ce=O, Dy, Tb
	L	**70**	70, **220**	70	70, 200	70, 200	70	70, 220	Dominated by STE, Gd and minor Dy, Tb
Aspedammen	H					323, **533**			Dominated Dy
	L				20, 150, **260**	**260**			Tb-Dy intense—transfers from Tb 495 nm @ 20 K to 485 nm Dy by 300 K
Hundholmen	H		600		**600**	**600**			Dominated by Tb, Dy
	L		20, 70			all			Dominated by 310 nm, Dy
Nedre Eivollen	H			650		323, 500, 625		525	Low intensity of emission in several RE
	L								Little emission

L are low temperature data (20–300 K); H are high temperature data (300–673 K). All temperature data are in K. The temperature of the strongest response in the samples is shown in bold. STE is the Self-Trapped Exciton (see text)

both experimental and theoretical grounds (Song and Williams 1996). The spectrum of Hundholmen at room temperature shows a ~320 nm peak (which we attribute to Gd³⁺—see below) but with a shoulder at 294 nm which decreases in intensity as the sample is heated above 50 K. We interpret this shoulder as direct emission from the V_k centre (Gorobets and Rogojine 2002).

A wide, well defined luminescence band at 380 nm occurs in many samples (NJH-16-39ppl, NJH-16-41grn, Aspedammen and Hundholmen), observed both at high and low temperatures. Defect related bands are often broad at low temperatures (T ~ 20 K) (FWHM average 64 nm for 280 nm in fluorite) due to the electron–phonon coupling typical for deep-level defects. Luminescence in the region 300–410 nm is attributed to several overlapping emissions from Ce³⁺, in which different centres have different intensities depending on how local charge balance is maintained. The splitting of the ground state (to $^2F_{7/2}$ and $^2F_{5/2}$) creates a characteristic doublet in the Ce³⁺ emission, which is located at 320 and 340 nm if the trivalent lanthanide is charge balanced by an interstitial F in a nearest neighbour position (e.g. Petit et al. 1981). If Ce³⁺ is adjacent to O²⁻, the Ce peaks shift to 350, 380 nm (Sunta 1983 and refs therein, Sils et al. 2009). This latter emission, around 380 nm, is seen in all the fluorite in the present study, except Nedre Eivollen (Fig. 3) and based on this, we infer that coupling of Ce³⁺ and oxide impurities occurs in our natural samples ($Ca^{2+} + F^- = Ce^{3+} + O^{2-}$).

Analysis of REE composition

Previous studies have shown differences in chondrite (C1)-normalised (McDonough and Sun 1995) REE compositional profiles in fluorite with Y plotted between Dy and Ho (Bau and Dulski 1995). The different profiles have been related to provenance. The fluorite from Norway shows negative europium and positive Y anomalies (cf. Gagnon et al. 2003) except Nedre Eivollen. They also show depletion in Light Rare Earth Elements (LREE) and an enrichment in HREE, typical of rare-earth rich fluorite of pegmatitic origin (Schönenberger et al. 2008; Czaja et al. 2012). The Aspedammen sample shows middle rare earth enrichment and a positive Y anomaly. NJH-16-41grn displays a slightly LREE enriched profile which is broadly flat at HREE with a negative Eu anomaly, typical of fluorites from alkaline nepheline syenites from early fluids/magmas (Schönenberger et al. 2008) while the other Greenland samples have incomplete profiles due to the low REE content.

REE profiles in minerals are the product of the REE concentrations of the fluid from which the fluorite crystallised and the partition coefficient for each lanthanide in the site. Figure 5 shows the chondrite-normalised REE profiles of the present sample suite as a function of ionic radius (Shannon and Prewitt 1970) of the RE^{3+} ion in eightfold coordination. Chondrite-normalised profiles of substituents into a single site should, in principle, be parabolic functions of ionic radius around a central 'optimum' radial distance (Blundy and Wood 1994). One may assume that the optimum radius of a lanthanide in the Ca site in fluorite is close to the ionic radius of Ca^{2+} in eightfold coordination (1.12 Å). In this case we would expect the fluorite structure to fit around the lanthanide ion, shrinking slightly for those ions that are smaller (HREE) or unchanged for the larger ones (LREE) for which the ionic radius and that of Ca^{2+} are similar.

Figure 5 shows the chondrite normalised REE profiles in the fluorite of the present study. NJH-16-41grn has a normalised REE profile with a maximum at ~1.08 Å, consistent with a 3% contraction from the 1.12 ionic radius of Ca^{2+} in the same coordination. Such values of contraction are consistent with the structural collapse observed when, for example, REE^{3+} substitutes in the Ca site in eudialyte (Borst et al. 2019). However, as ΣREE increases (e.g. Aspedammen), a smaller optimum REE-O optimum distance (1.04 Å) is observed. In the two yttrofluorites, Hundholmen and Nedre Eivollen, the smallest rare earths are accommodated most easily, indicating an optimum radius ≤ 0.98 Å. These different profiles can be interpreted either as differences in the REE-profile of the fluid from which the fluorite formed (i.e. partition coefficients are nearly constant, Payne et al. 2023), or that partition coefficients change as the lanthanide content increases. The first explanation would require that

later fluids evolved from LREE to HREE enrichment with time (Möller et al. 1976; Kempe et al. 1999; Schwinn and Markl 2005; Trinkler et al. 2005) and falling temperature (Williams-Jones et al. 2012) and are the way that many previous authors have interpreted such observations. However, we propose a simpler explanation, i.e. as lanthanide concentrations in natural fluorite increase, lanthanide ions cluster, locally reducing the size of the coordination sphere of the metal. Since the size of the crystallographic site controls the partition coefficients, such clustering would cause the optimum REE profile to move from LREE- to HREE-enriched profiles. Such a mechanism is observed in tveitite, which has a distorted fluorite-derived structure and interstitial F, but with smaller REE sites (Bevan et al. 1982). The average ionic radius of the RE^{3+} in tveitite is 0.98 Å, indicating that the formation of tveitite-type domains in fluorite would reduce the radius of the RE site. In addition to the change in the optimum rare earth in the fluorite, we observe changes in the cell parameters (Fig. 1, Table 2). Initially the unit cell shrinks as REE are substituted, but then when the total rare earth content ~ 2000 ppm, the unit cells expand linearly with REE content. Our chemical and crystallographic data are consistent with a model in which REE initially substitute ideally, but then progressive REE substitution in fluorite triggers lanthanide ordering. At low concentrations RE ions in fluorite are isolated and substitute directly for Ca^{2+} and, therefore,s have parabolic profiles centred around 1.08 Å. Ideal substitution of smaller lanthanide ions for Ca^{2+} causes the cell parameters to shrink. However, as the concentration increases, lanthanide ions cluster into localised RE-rich domains in which the optimum RE ionic radius is smaller, thereby creating profiles which favour heavy rare earths. The unit cell of tveitite (Bevan et al. 1982) is derived
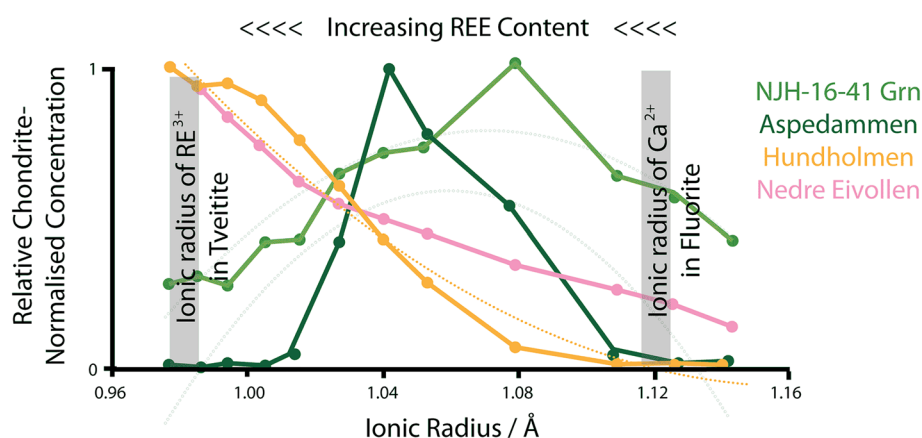
Fig. 5 Chondrite Normalise REE profiles for Fluorite in the Present Study, with the highest point of each graph normalised to 1. Data are shown only for lanthanides with f electrons (i.e. not La and Y) and elements whose concentrations are significantly above the limit of detection. The ionic radius of the Ca site in fluorite and the RE-site in tveitite are shown. The maximum in each fluorite profile migrates towards smaller radii as the overall REE concentration increases. The colours of the lines are the same as in Fig. 1 and represent the colour of the sample in hand specimen. The profile of NJH-16-39ppl could not be drawn since most REE are < lod

from fluorite but is larger; whereas fluorite accommodates a metal ion for every 40.9 $\mathring{A}^3$ of the unit cell in fluorite, tveitite accommodates each metal in (on average) 42.6 $\mathring{A}^3$, i.e. an expansion of the unit cell volume by 4%. Hence our model would predict that cell parameters shrink during ideal substitution of a smaller ion, but then expand when HREE-rich tveitite clusters form.

Features attributable to luminescence from lanthanide ions

All trivalent lanthanide ions are luminescent (except for La and Lu) with emission lines ranging from the UV (Gd) though visible (e.g. Er, Tb, Dy) and into the near-infrared (Nd) (Hagemann et al. (2022). REE display diagnostic narrow wavelength emissions, with some broadening caused by interaction with the lattice, due to the shielding of the 4f electrons on the inner shells by the 5-s and 5-p subshells (Dieke and Crosswhite 1963). To a first order approximation, it is often assumed that interaction between the 4f electrons and the lattice is minimal (cf. Gaft et al. 2015) but that local coordination symmetry can influence the expression and relative intensities of the emission lines.

The sample with the lowest REE concentration, NJH-16-39ppl (ΣREE = ~ 30 ppm), has luminescence dominated by defects in the UV (particularly the self-trapped exciton at 280 nm) with very little contribution that can be attributed to REE ions. We infer that the concentrations of physical defects in NJH-16-39ppl exceed the concentration of lanthanides. While most broad UV emissions in fluorite are linked to intrinsic lattice defects, the sharp lines are attributed to intra-ion energy cascades within lanthanide ions, particularly Gd^{3+} (312 nm), Dy (485, 580 nm) and Tb (490, 540, 585 nm). Gaft and Raichlin (2020) showed that Pr^{3+} luminescence in fluorite is hidden behind stronger Sm and Dy emissions and this is also possible in our samples. The sharp lines are visible in most samples, including NJH-16-41grn (ΣREE = ~ 400 ppm). Lanthanide-related emissions in fluorite are found at both cryogenic and high (i.e. above 300 K) temperatures and the strongest lanthanide emission in the fluorite system is typically from Dy^{3+} at 485 nm. During XEOL, energy is deposited at high (keV) energies onto the lattice and the energy returns to the ground state via a sequence of energy cascades. We interpret the dominance of Gd, Dy and Tb in fluorite luminescence to indicate that energy levels in those ions have the greatest energy cross-section (and therefore interact most efficiently) with the fluorite lattice. Dy and Tb show emission lines at multiple wavelengths due to the spin orbit coupling of the emitting ions (Dieke and Crosswhite 1963).

Luminescence is a complex but subtle probe of local coordination and we use the luminescence data to explore coordination state. Figure 6 plots the intensity of the Dy
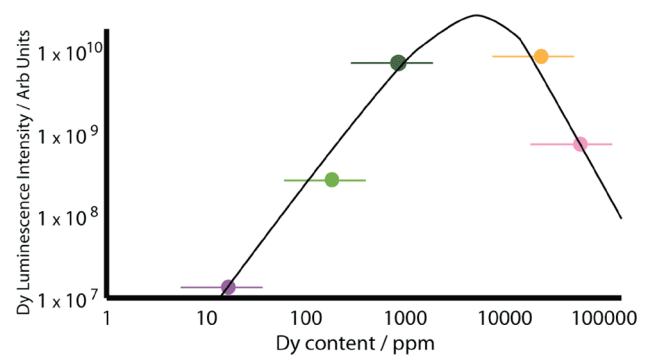
Fig. 6 Concentration of Dy versus Intensity of Dy Luminescence. Colours correspond to samples in Fig. 1. The Intensity broadly increases linearly with concentration until ~ 1000 ppm at which point the intensity drops. The intensity is estimated as the integral of the 480 nm emission between 75 and 125 K for each sample

emission against Dy composition. The relationship is linear up to Dy = ~ 1000 ppm, at which point further substitution results in a progressive decrease in luminescence intensity. Since the luminescence intensity is linearly dependent on composition at low (< 1000 ppm) concentrations, we infer that the Dy^{3+} ions are isolated at these compositional ranges and concentrations of the luminophore are linearly proportional to luminescence intensity. However, the intensity of the most RE-rich fluorites (Hundholmen and Nedre Eivollen) is less than that of samples with lower REE concentrations (Fig. 6). These observations suggest that lanthanide substitution occurs not as isolated ions. This could come about as total lanthanide composition increases, enhancing the probability that lanthanide ions are sited next to each other in the structure and therefore can interact. However the coincident shift in the optimum lanthanide radius to smaller values indicates that the lanthanides are clustering to minimise total lattice strain (Townsend and White 1996; Townsend et al. 2001), leading to the formation of complex point defects such as four interstitials, three vacancies and two interstitial impurity ions grouped together; described as 4:3:2 (Calderon et al. 1992). We interpret the drop in luminescence intensity at high concentrations to result from the lanthanide ions above ~ 1000 ppm act behaving as clusters and that localised energy transfer between lanthanides creates a reduction of the overall quantum efficiency of luminescence, as observed in REE-doped synthetic CaF_2 (Holgate et al. 1994; Wang et al. 2017).

The luminescence data and the chondrite-normalised rare earth profiles are both consistent with a model in which, at low concentrations, lanthanide ions are isolated, creating local distortions and defects from the need to balance charge. As the lanthanide concentrations increase (> ~ 1000 ppm), fluorite accommodates lanthanides in clustered forms, resulting in smaller bond distances which facilitate inter-ion

energy transfer and hence reduce luminescence quantum efficiencies. Natural samples, with geological timescales over which to acquire perfect states of defect order, are exceptional materials in which to explore defect coupling and ordering.

Conclusions

We have measured the chemical composition and X-ray Excited Optical Luminescence (XEOL) of a suite of natural, rare earth-containing fluorites to explore the relationship between the composition and luminescence as a function of temperature. Natural fluorite demonstrates luminescence responses that are attributed to structural defects and intra-ion energy cascades involving REE^{3+} ions. When total REE compositions are low, XEOL from structural defects in the UV dominate, particularly the self-trapped exciton at 280 nm. When REE concentrations increase, luminescence from Dy^{3+} and Tb^{3+} dominate the spectra. The dependence of luminescence intensity on lanthanide composition increases linearly until ~ 1000 ppm at which point, intensity falls. The compositional and luminescence data provide a consistent model in which lanthanide substitution in fluorite at low concentrations (e.g. < 1000 ppm) occurs as isolated centres with charge offsets mediated by interstitial fluorides and electronic point defects. In this region, luminescence intensity of the lanthanide emissions is broadly a linear function of lanthanide composition. Above ~ 1000 ppm, intensity falls as a function of composition. Chondrite-normalised lanthanide profiles show that smaller (heavier) rare earths become incorporated more easily into fluorite as the total rare earth content increases. We interpret the changing REE-profiles in fluorite as lanthanide clustering as total REE content increases. The clusters have smaller lanthanide sites, resulting both in a shift to smaller RE–O bond distances (favouring heavy rare earths and Y) and reduced luminescence quantum efficiency. Such a model explains both the luminescence intensity behaviour and the prevalence of heavy REE in fluorite. These centres are particularly visible in natural fluorite since it has geological timescales over which to acquire perfect states of defect order.

Declarations

References

Agulló-López F, Catlow CRA, Townsend PD (1988) Point defects in materials. Academic Press, London

Aoki T, Garvie L, Rez P (2015) Observation of color center peaks in calcium fluoride. Ultramicroscopy 153:40–44

Assylbayev R, Lushchik A, Lushchik C, Kudryavtseva I, Shablonin E, Vasil'Chenko E, Akilbekov A, Zdorovets M (2018) Structural defects caused by swift ions in fluorite single crystals. Opt Mater 75:196–203

Bartram R, Stoneham A (1975) On the luminescence and absence of luminescence of F centers. Solid State Commun 17:1593–1598

Bau M, Dulski P (1995) Comparative study of yttrium and rare-earth element behaviours in fluorine-rich hydrothermal fluids. Contrib Miner Petrol 119:213–223

Bergstøl S, Jensen BB, Neumann H (1977) Tveitite, a new calcium yttrium fluoride. Lithos 10:81–87

Betts D, Townsend P (1993) Temperature distribution in thermoluminescence experiments. II. Some calculational models. J Phys D Appl Phy 26:849

Bevan DJM, Strahle J, Greis O (1982) The crystal structure of tveitite, an ordered yttrofluorite mineral. J Solid State Chem 44:75–81

Bill H, Calas G (1978) Color centers, associated rare-earth ions and the origin of coloration in natural fluorites. Phys Chem Miner 3:117–131

Blundy J, Wood B (1994) Prediction of crystal-melt partition coefficients from elastic moduli. Nature 372:452

Borst AM, Finch AA, Friis H, Horsburgh NJ, Gamaletsos PN, Göttlicher J, Steininger R, Geraki K (2019) Structural state of rare earth elements in eudialyte-group minerals. Mineral Mag. https://doi.org/10.1180/mgm.2019.50

Calderon T, Khanlary M-R, Rendell H, Townsend P (1992) Luminescence from natural fluorite crystals. Int J Radiat Appl Instrum Part D Nucl Tracks Radiat Meas 20:475–485

Chang LLY, Howie RA, Zussman J (1996) Rock forming minerals: non-silicates; sulphates, carbonates, phosphates, halides. Harlow (Longman), 383 pp, ISBN 0-582-30093-2

Cheetham AK, Fender BEF, Cooper MJ (1971) Defect structure of calcium fluoride containing excess anions: I. Bragg Scattering. J Phys C: Solid St Phys 4:3107–3121

Cooper MA, Abdu YA, Ball NA, Černý P, Hawthorne FC, Kristiansen R (2012) Aspedamite, ideally $\square_{12}(Fe^{3+}, Fe^{2+})_3Nb_4[Th(Nb, Fe^{3+})_{12}O_{42}]\{(H_2O),(OH)\}_{12}$, a new heteropolyniobate mineral species from the Herrebøkasa Guarry, Aspedammen, Østfold, Southern Norway: description and crystal structure. Can Mineral 50:793–894

Czaja M, Bodył-Gajowska S, Lisiecki R, Meijerink A, Mazurak Z (2012) The luminescence properties of rare-earth ions in natural fluorite. Phys Chem Miner 39:639–648

Dieke GH, Crosswhite H (1963) The spectra of the doubly and triply ionized rare earths. Appl Opt 2:675–686

Dill H, Weber B (2010) Variation of color, structure and morphology of fluorite and the origin of the hydrothermal F-Ba deposits at Nabburg-Wölsendorf, SE Germany. Neues Jahrbuch Für Mineralogie-Abhandlungen J Mineral Geochem 187:113–132

Dunkl I, Mikes T, Simon K, Von Eynatten H (2008) Brief introduction to the Windows program Pepita: data visualization, and reduction, outlier rejection, calculation of trace element ratios and concentrations from LA-ICP-MS data. Mineralogical Association of Canada Short Course, Vancouver

Ege A, Wang Y, Townsend P (2007) Systematic errors in thermoluminescence. Nucl Instrum Methods Phys Res, Sect A 576:411–416

Eggins SM, Rudnick RL, Mcdonough WF (1998) The composition of peridotites and their minerals: a laser-ablation ICP-MS study. Earth Planet Sci Let 154:53–71

Finch AA, Goodenough K, Salmon H, Andersen T (2001) The petrology and petrogenesis of the North Motzfeldt Centre, Gardar Province, South Greenland. Mineral Mag 65:759–774

Finch AA, McCreath JA, Reekie CDJ, Hutchison W, Ismaila A, Armour-Brown A, Andersen T, Simonsen SL (2019a) From Mantle to Motzfeldt: a genetic model for syenite-hosted Ta, Nb-mineralisation. Ore Geol Rev 107:402–416

Finch AA, Wang Y, Townsend PD, Ingle M (2019b) A high sensitivity system for luminescence measurement of materials. Luminescence 34:280–289

Gaft M, Raichlin Y (2020) Luminescence of 5d–4f transitions of Pr^{3+} in natural fluorite CaF_2, anhydrite $CaSO_4$ and apatite $Ca_5(PO_4)_3F$. Phys Chem Min 47(1):5. https://doi.org/10.1007/s00269-019-01074-6

Gaft M, Reisfeld R, Panczer G (2015) Modern luminescence spectroscopy of minerals and materials. Springer, London

Gagnon JE, Samson IM, Fryer BJ, Williams-Jones AE (2003) Compositional heterogeneity in fluorite and the genesis of fluorite deposits: insights from LA–ICP–MS analysis. Can Mineral 41:365–382

Gorobets BS, Rogojine AA (2002) Luminescent spectra of minerals Moscow, RPC VIMS

Hagemann H, Ayoubipour S, Delgado T, Schnyder C, Gnos E (2022) Probing luminescence of rare earth ions in natural pink fluorites using Raman microscopes. J Raman Spectrosc 53(8):1464–1470. https://doi.org/10.1002/jrs.6383

Holgate S, Sloane T, Townsend P, White D, Chadwick AV (1994) Thermoluminescence of calcium fluoride doped with neodymium. J Phys Condens Matter 6:9255

Kempe U, Monecke T, Oberthür T, Kremenetsky A (1999) Trace elements in scheelite and quartz from the Muruntau/Myutenbai gold deposit (Uzbekistan): Constraints on the nature of the ore-forming fluids. In: Mineral deposits: processes to processing. Balkema, Rotterdam, pp 373–376

Lopez F, Aguilar M, Jaque F, Agulló-López F (1980) Thermoluminescence and recovery processes in pure and doped NaCl after 20 K irradiation. Solid State Commun 34:869–872

McDonough WF, Sun SS (1995) The composition of the Earth. Chem Geol 120:223–253

McKeever S, Chen R (1997) Luminescence models. Radiat Meas 27:625–661

Möller P, Parekh P, Schneider H-J (1976) The application of Tb/Ca–Tb/La abundance ratios to problems of fluorspar genesis. Miner Depos 11:111–116

Müller A, Husdal T, Sunde Ø, Friis H, Andersen T, Johansen TS, Werner R, Thoresen Ø, Olerud S (2017) Geological guides 6-2017

Oberti R, Ottolini L, della Ventura G, Parodi GC (2001) On the symmetry and crystal chemistry of britholite: new structural and microanalytical data. Am Mineral 86:1066–1075

Payne MR, Gysi AP, Hurtig NC (2023) Hydrothermal fluorite solubility experiments and mobility of REE in acidic to alkaline solutions from 100 to 250 °C. Chem Geol 617:121256

Pekov IV, Chukanov NV, Kononkova NN, Yakubovich OV, Massa W, Voloshin AV (2009) Tveitite-(Y) and REE-enriched fluorite from amazonite pegmatites of the Western Keivy, Kola Peninsula, Russia: Genetic crystal chemistry of natural Ca, REE-fluorides. Geol Ore Deposits 51:595–607

Petit R, Evesque P, Duran J (1981) Dimers and clusters in $CaF_2:Pr^{3+}$. Laser selective excitation and time-resolved spectroscopy. J Phys C Solid State Phys 14:5081

Popov A, Kotomin E, Maier J (2017) Analysis of self-trapped hole mobility in alkali halides and metal halides. Solid State Ionics 302:3–6

Pouchou LJ, Pichoir F (1984) New model quantitative X-ray microanalysis, 1. Application to the analysis of homogeneous samples. Rech Aerosp 3:13–38

Romer R, Kjøsnes B, Korneliussen A, Lindahl I, Skyseth T, Stendal M, Sundvoll B (1992) The Archaean-Proterozoic boundary beneath the Caledonides of northern Norway and Sweden: U–Pb, Rb–Sr and Nd isotopic data from the Rombak-Tysfjord area. NGU Rep 91:67

Schönenberger J, Köhler J, Markl G (2008) REE systematics of fluorides, calcite and siderite in peralkaline plutonic rocks from the Gardar Province, South Greenland. Chem Geol 247:16–35

Schwinn G, Markl G (2005) REE systematics in hydrothermal fluorite. Chem Geol 216:225–248

Shannon RD, Prewitt CT (1970) Revised values of effective ionic Radii. Acta Crystallogr A B26:1046

Sils J, Hausfeld S, Clauß W, Pahl U, Lindner R, Reichling M (2009) Impurities in synthetic fluorite for deep ultraviolet optical applications. J Appl Phys 106:063109

Song K, Williams RT (1996) Self-trapped excitons. Springer, London

Stokes GG (1852) On the change of refrangibility of light. Philos Trans R Soc Lond 142:463–562

Stoneham AM (2001) Theory of defects in solids: electronic structure of defects in insulators and semiconductors. Oxford University Press, Oxford

Sunta CM (1983) Irradiation effects on Ce^{3+} thermoluminescence centres of mineral CaF_2. Radiat Effects 79:149–158

Sverdrup TL (1968) Yttrofluorite–yttrocerite–cerfluorite in Norwegian pegmatites. Norsk Geol Tidsskr 48:245–252

Townsend PD, Kelly JC (1973) Color Centres and Imperfections in Insulators and Semiconductors. Crane, Russak

Townsend PD, White D (1996) Interpretation of rare earth thermoluminescence spectra. Radiat Prot Dosimetry 65:83–88

Townsend PD, Rowlands A, Corradi G (1997) Thermoluminescence during a phase transition. Radiat Meas 27:31–36

Townsend PD, Jazmati A, Karali T, Maghrabi M, Raymond S, Yang B (2001) Rare-earth-size effects on thermoluminescence and second-harmonic generation. J Phys: Condens Matter 13:2211

Trinkler M, Monecke T, Thomas R (2005) Constraints on the genesis of yellow fluorite in hydrothermal barite–fluorite veins of the Erzgebirge, Eastern Germany: evidence from optical absorption spectroscopy, rare-earth-element data, and fluid-inclusion investigations. Can Mineral 43:883–898

Upton BGJ (2013) Tectono-magmatic evolution of the younger Gardar southern rift, South Greenland. Geolog Surv Denmark Greenland Bull 29:1

Upton, BGJ, Emeleus CH, Heaman LM, Goodenough KM, Finch AA (2003) Magmatism of the mid-Proterozoic Gardar Province, South Greenland: chronology, petrogenesis and geological setting. Lithos, 68:43–65

Valeur B, Berberan-Santos MN (2011) A brief history of fluorescence and phosphorescence before the emergence of quantum theory. J Chem Educ 88:731–738

Vogt T (1923) Über die seltenen Erden im Yttrofluorit von Hundholmen. Centralblatt für Mineralogie Geologie und Paläontologie 1923:673–676

Wang Y, Zhao Y, White D, Finch AA, Townsend PD (2017) Factors controlling the thermoluminescence spectra of rare earth doped calcium fluoride. J Lumin 184:55–63

Williams-Jones AE, Samson IM, Migdosov A (2012) Hydrothermal mobilisation of the rare earth elements—a tale of ceria and yttria. Elements 8:355–360

Yang B, Townsend P, Rowlands A (1998) Low-temperature thermoluminescence spectra of rare-earth-doped lanthanum fluoride. Phys Rev B 57:178